ARTICLE OPEN

Check for updates

Probing two-qubit capacitive interactions beyond bilinear regime using dual Hamiltonian parameter estimations

Jonginn Yun[1,4], Jaemin Park[1,4], Hyeongyu Jang[1], Jehyun Kim[1], Wonjin Jang[1], Younguk Song[1], Min-Kyun Cho[1], Hanseo Sohn[1], Hwanchul Jung[2], Vladimir Umansky[3] and Dohun Kim[1]✉

We report the simultaneous operation and two-qubit-coupling measurement of a pair of two-electron spin qubits, actively decoupled from quasi-static nuclear noise in a GaAs quadruple quantum dot array. Coherent Rabi oscillations of both qubits (decay time ≈2 μs; frequency few MHz) are achieved by continuously tuning their drive frequency using rapidly converging real-time Hamiltonian estimators. We observe strong two-qubit capacitive interaction (>190 MHz), combined with detuning pulses, inducing a state-conditional frequency shift. The two-qubit capacitive interaction is beyond the bilinear regime, consistent with recent theoretical predictions. We observe a high ratio (>16) between coherence and conditional phase-flip time, which supports the possibility of generating high-fidelity and fast quantum entanglement between encoded spin qubits using a simple capacitive interaction.

npj Quantum Information (2023)9:30 ; https://doi.org/10.1038/s41534-023-00699-4

INTRODUCTION

Spins in semiconductor quantum dot (QD) nanostructures offer a promising platform for realizing scalable quantum information-processing units with high-fidelity universal quantum control[1–3]. Recent progress in III–V and IV semiconducting materials demonstrated several achievements including the demonstration of single- and two-qubit gate fidelities exceeding 99% in ^{Nat}Si and ^{28}Si (ref. [2,3]), simultaneous qubit operations in GaAs with a coherence time over 2 μs (refs. [4,5]), a few qubit entanglements in Ge and ^{28}Si (refs. [6–8]), high-temperature operations of spin qubits[9–11], and long-range coupling of spin qubits using superconducting cavity structures[12,13]. The field is currently moving towards the high-fidelity control of multiple qubits and the generation of controlled entanglement.

However, low-frequency noise, including quasi-static nuclear fluctuation and slow charge noise, is one of the main factors reducing coherence times below the intrinsic limit of a given host material[14–20]. For example, the spin coherence time is often affected by charge noise coupled through the inhomogeneous magnetic field generated by micromagnets[18,19]. In addition, exchange- or capacitive-coupling-based two-qubit control is inherently susceptible to charge noise[14,16,20–22]. Thus, eliminating or mitigating slow magnetic and electric noises is an important task in semiconductor QD platforms.

Real-time Hamiltonian parameter estimation and measurement-based feedback[4,23,24] are two complementary techniques to coherent quantum feedback[25] capable of error mitigation, which is compatible —albeit sequentially—with general qubit controls. Previously, the Hamiltonian parameter estimation applied to GaAs has shown that the effect of quasi-static nuclear spin fluctuations can be strongly suppressed for single-spin[23] and singlet–triplet (ST_0) qubits[4]. Nevertheless, extending the technique to a multi-qubit system is desirable. While this has not been demonstrated to date, the simultaneous Hamiltonian estimation is also crucial for the accurate measurement of inter-qubit coupling strength. This is particularly important in the case of GaAs, for which the application of real-time calibrated single-qubit rotations on each qubit is a prerequisite.

In this study, we demonstrate the simultaneous drive of a pair of ST_0 qubits in GaAs. The quasi-static nuclear noise for each qubit is actively decoupled using a Bayesian inference-based real-time Hamiltonian estimation circuit. We show high-quality Rabi oscillations for both qubits with an oscillation quality factor above 10. We further exploit this result to demonstrate the measurement of the electrostatic coupling of two ST_0 qubits, which grows beyond an empirically assumed bilinear form[26,27] for large intra-qubit exchange energies. Combining this with the spin-echo sequence, we assess the potential to generate a high-fidelity and fast conditional phase gate using capacitive interactions in a linear QD array.

RESULTS

Simultaneous Hamiltonian parameter estimation

Figure 1a shows a quadruple QD device on top of a GaAs/AlGaAs heterostructure, hosting a pair of ST_0 qubits with singlet $|S\rangle$ and triplet-zero $|T_0\rangle$ basis states (See methods section and ref. [28] for details of the material structure and device fabrication). High-frequency and synchronous voltage pulses, combined with DC voltages through bias-tees, were input to gates V_1–V_6. Fast dual RF reflectometry was performed by injecting a carrier signal having a frequency ≈125 MHz (153 MHz) and power of −100 dBm at the Ohmic contacts of the left (right) RF single-electron transistors (see Fig. 1a). The reflected power was monitored through a frequency-multiplexed homodyne detection. The device was operated in a dilution refrigerator with a base temperature≈ $7mK$, where an external magnetic field (0.7 T) was applied in the direction shown in Fig. 1a. The measured electron temperature is ≈72 mK (ref. [28]).

[1]Department of Physics and Astronomy, and Institute of Applied Physics, Seoul National University, Seoul 08826, Korea. [2]Department of Physics, Pusan National University, Busan 46241, Korea. [3]Braun Center for Submicron Research, Department of Condensed Matter Physics, Weizmann Institute of Science, Rehovot 76100, Israel. [4]These authors contributed equally: Jonginn Yun, Jaemin Park. ✉email: dohunkim@snu.ac.kr

The Hamiltonian of the two-qubit system is given (up to a constant term) by[26]

$$H=\frac{J_L(\varepsilon_L)}{2}\sigma_{zL}\otimes I+\frac{\Delta B_{zL}}{2}\sigma_{xL}\otimes I+\frac{J_R(\varepsilon_R)}{2}I\otimes\sigma_{zR}+\frac{\Delta B_{zR}}{2}I\otimes\sigma_{xR}+\frac{J_{RL}(\varepsilon_L,\varepsilon_R)}{2}(\sigma_{zL}-I)\otimes(\sigma_{zR}-I) \quad (1)$$

where $J_L(\varepsilon_L)(J_R(\varepsilon_R))$ is the exchange splitting between states $|S\rangle$ and $|T_0\rangle$, controlled by potential detuning $\varepsilon_L(\varepsilon_R)$ of the left (right) qubit (Q_L and Q_R). $\sigma_{i=xL,zL}(\sigma_{i=xR,zR})$ is the Pauli matrix for Q_L (Q_R), I is the identity matrix, and ΔB_{zL} (ΔB_{zR}) is the magnetic field difference between the constituent QDs of each qubit, set by the local hyperfine interaction with the host Ga and As nuclei. Here, we adopted $g^*\mu_B/h=1$ for units, where $g^*\approx-0.44$ is the effective gyromagnetic ratio in GaAs, μ_B is the Bohr magneton, and h is Planck's constant.

For the real-time Hamiltonian estimation of the quasi-static fluctuations of ΔB_{zL} and ΔB_{zR}, owing to statistical fluctuations of the nuclei, we extended the methodology developed in refs. [4,23,28] for two-qubit systems. Briefly, we initialized and measured the $(2,0)_L$ ($(0,4)_R$) charge configuration for Q_L (Q_R), respectively, via fast energy selective tunneling (EST)-based single-shot readout and adaptive initialization[29–31] (see also Supplementary Note 1). In contrast to previous studies, in which sequential measurements were performed using the Pauli spin blockade (PSB)-based readout[26,32], here we simultaneously measured both qubits to minimize the estimation latency. During the estimation sequence, when qubits are in the evolution step, $J_L(\varepsilon_L)$, $J_R(\varepsilon_R)$, and $J_{RL}(\varepsilon_L,\varepsilon_R)$ are abruptly turned off. Each qubit evolves around the x axis of the respective Bloch sphere during the evolution time $t_k=1.67$ k ns at the kth estimation trial (Fig. 1b). For each simultaneous single-shot measurement, the Bayesian inference is simultaneously performed according to the following rule (up to a normalization constant)[4]

$$P(\Delta B_{zi}|m_{Ni},m_{(N-1)i},\ldots m_{1i})=P_0(\Delta B_{zi})\prod_{k=1}^{N}\frac{1}{2}[1+r_{ki}(\alpha+\beta\cos(2\pi\Delta B_{zi}t_{ki}))],\ \text{for } i=L,\ R, \quad (2)$$

where N is the number of single-shot measurements per Hamiltonian estimation, $P_0(\Delta B_{zi})$ is the uniform initial distribution, $r_{ki}=1(-1)$ for $m_{ki}=|S\rangle(|T_0\rangle)$, and $\alpha=0.1(\beta=0.8)$ is the parameter determined by the axis of rotation on the Bloch sphere (oscillation visibility). After the Nth round, the value of ΔB_{zi} is estimated, where the posterior distribution $P(\Delta B_{zi}|m_{Ni},m_{(N-1)i},\ldots m_{1i})$ reaches its maximum. The Bayesian circuit was implemented using a commercial field-programmable gate array (FPGA)[4] (see Supplementary Note 2).

Figure 1c shows a typical time trace of the estimated ΔB_{zL} and ΔB_{zR}. The time resolution of these estimations is ~1.8 ms, which consists of $(N=70)\times26$ µs, where a single Bayesian update takes 16 µs and 10 µs for a single-shot measurement and calculation according to Eq. (2), respectively. We found that both ΔB_zs exhibit nonzero average values, likely arising from unintentional nuclear polarization, as reported previously for similarly prepared GaAs devices[17,33]. When ensemble-averaged, this fluctuation leads to a nuclear fluctuation-limited coherence time T_2^* of the order of 20 ns. Moreover, the difference between the mean values of ΔB_{zL} and ΔB_{zR} is at least twice the standard deviation. While the microscopic origin of this phenomenon is not well known yet, we used this difference to set the range of qubit frequencies to $25<\Delta B_{zL}<50$ ($100<\Delta B_{zR}<160$) MHz for simultaneous qubit drive and active frequency feedback.

As shown in the inset of Fig. 2a, we concatenate the Bayesian estimators, acting as probe and operation steps, to control the two qubits in the frequency feedback mode. The controller triggers the operation step when the estimated ΔB_z in the probe step is in the range described above; otherwise, the cases are discarded. However, the preset range of allowed ΔB_z covers almost the entire distribution (Fig. 1c), so heralding does not significantly increase the total experimental time. When triggered, each qubit is first adiabatically initialized near the x axis on the Bloch sphere. The controller also adjusts the RF drive frequency using the probed ΔB_z for each qubit. Then, an RF pulse, with a varied pulse length, is applied to gate V_2 (V_5) to resonantly modulate J_L (J_R) and

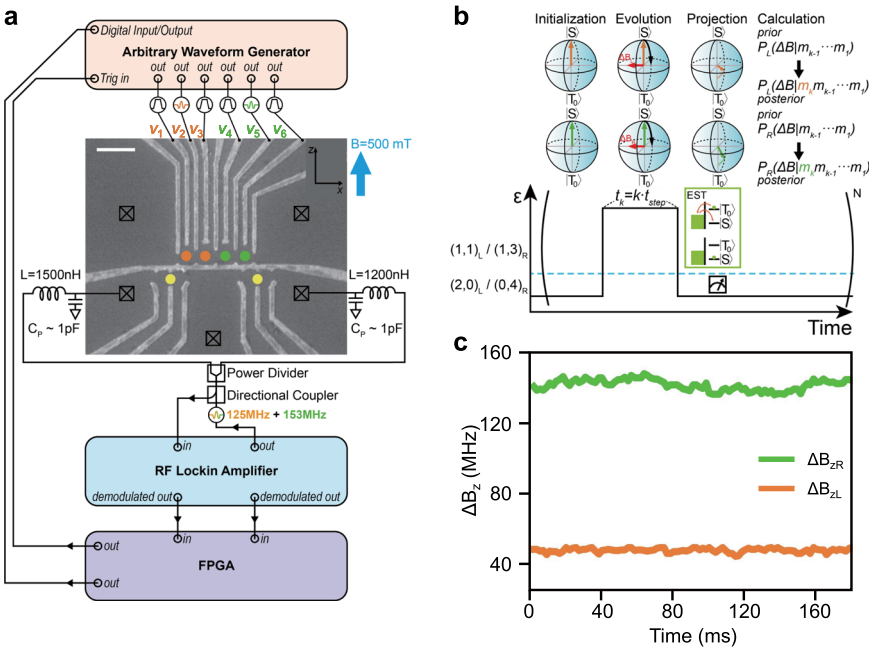

Fig. 1 Experimental setup. a A schematic of the experimental setup. Yellow circles indicate the RF single-electron transistors for dual RF reflectometry. Orange (green) circles indicate QDs for the left (right) ST_0 qubit (Q_L and Q_R). The plunger and barrier gates are connected to the arbitrary waveform generator for the application of detuning and RF pulses. The white scale bar corresponds to 500 nm. **b** Schematic diagram of the dual Hamiltonian estimation of the field gradient ΔB_L and ΔB_R. See main text for the estimation procedure. The green box shows the energy selective tunneling-based single-shot readout method. **c** The example traces of the simultaneously estimated field gradient ΔB of each qubit as a function of time.

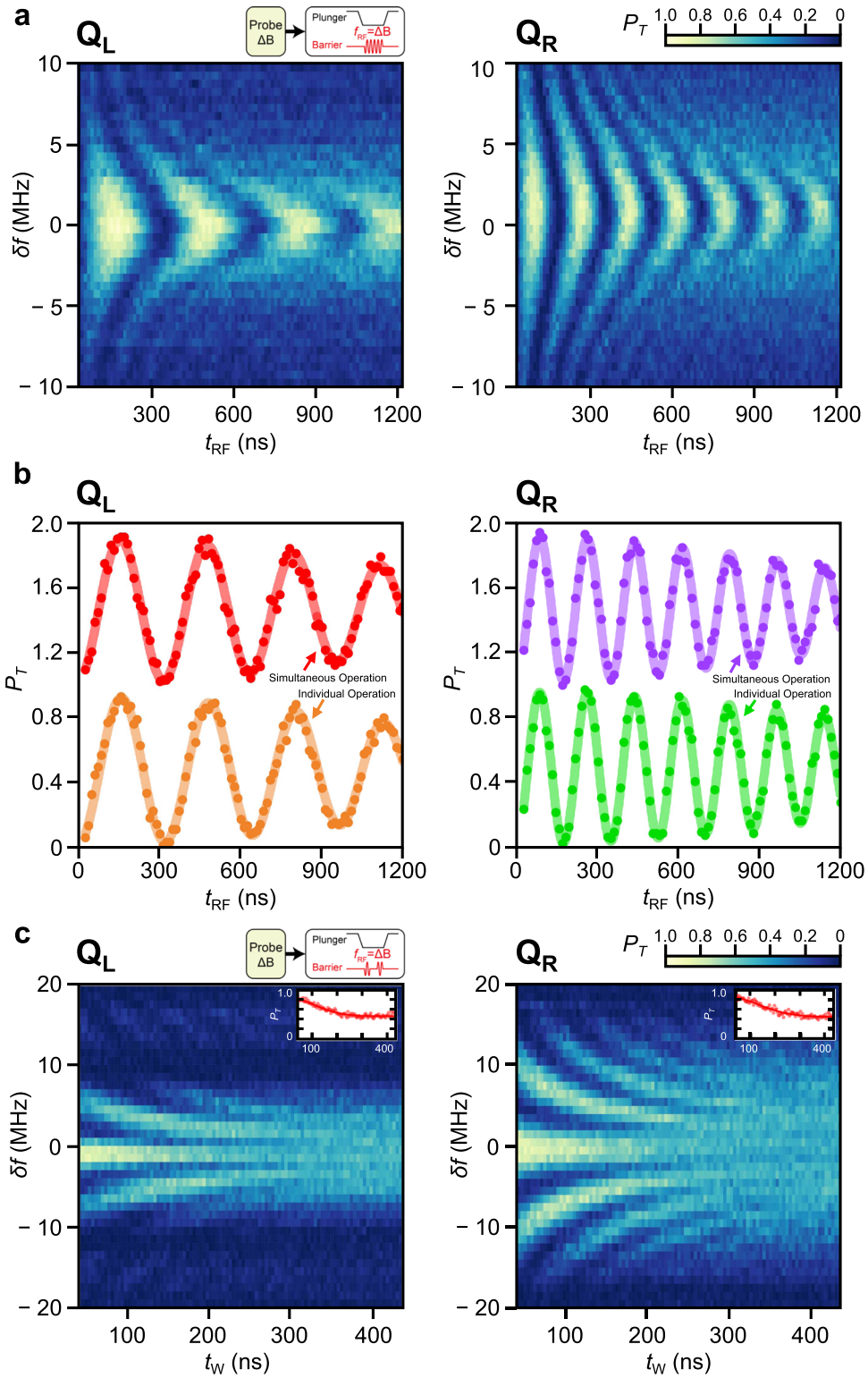

Fig. 2 Simultaneous driving of two ST_0 qubits. a Individually driven Rabi oscillation of the triplet return probability P_T of Q_L and Q_R as a function of controlled detuning δf and RF pulse duration t_{RF}. **b** The representative P_T oscillation of each qubit as a function of RF pulse duration for an individual and simultaneous operation. Solid curves are a fit to sinusoidal functions with a Gaussian envelope. **c** Ramsey fringe of P_T as a function of controlled detuning δf and Ramsey delay t_W, showing a typical Ramsey interference pattern. Inset: the line cut at the resonance condition. The solid curve is a fit to a Gaussian decay function $P_T(t_W) = A\exp(-(t_W/T_2^*)^2) + B$ with the best fit parameter $T_2^* \approx 151$ (183) ns for Q_L (Q_R).

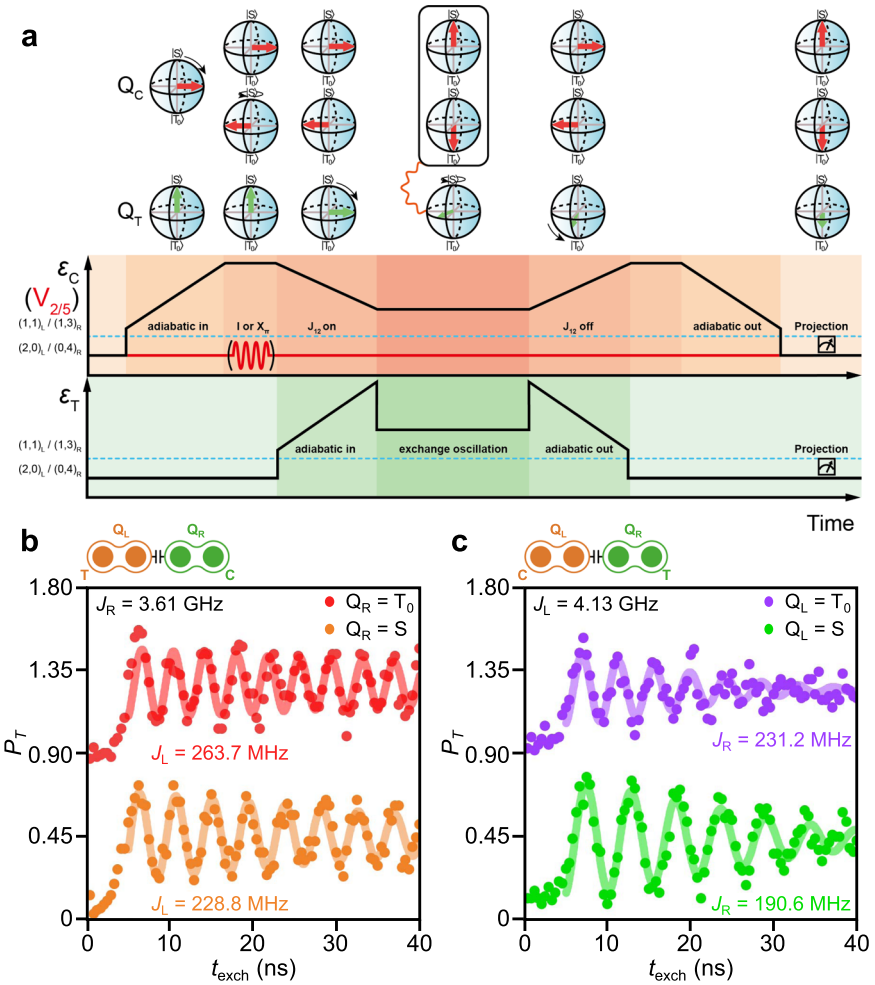

Fig. 3 Demonstration of inter-qubit coupling. a A pulse sequence to produce the control qubit (Q_C) state-dependent exchange oscillation of the target qubit (Q_T). A schematic illustration of the state of both qubits in each step is depicted in the upper panel. **b**, **c** The exchange oscillations of Q_L (Q_R) depending on the state of the other qubit as control. The lower and upper traces are measured when the state of Q_T is $|S\rangle$ and $|T_0\rangle$, respectively.

induce Rabi oscillation. In all experiments, ~50 shots of operations were performed after one probe step.

The main panel of Fig. 2a shows the coherent Rabi oscillation for each qubit measured as a function of the RF pulse duration t_{RF} and the controlled detuning δf with respect to the actively adjusted resonant frequency. The chevron pattern of Q_R shows a resonance frequency shift, most likely caused by the AC stark effect[34]. Figure 2b compares the Rabi oscillations for individual and simultaneous qubit operations under resonant conditions. For the former (latter), both the probe and RF pulses were applied to only one qubit (simultaneously on both qubits). For individual operations, Q_L (Q_R) shows a Rabi decay time $T_{Rabi} = 1.75$ μs (1.88 μs) at the Rabi frequency $f_{Rabi} = 3.09$ MHz (5.69 MHz) and oscillation visibility of 90.8% (93.6%), yielding the oscillation quality factor $Q = f_{Rabi} T_{Rabi} \approx 5\ (11)$. For simultaneous operations, corresponding results are 1.68 μs (1.59 μs), 3.12 MHz (5.68 MHz), and 88.4% (88.9%).

The comparison reveals that the Rabi frequency remains virtually unchanged regardless of the operation scheme, indicating a negligible RF crosstalk between the two qubits. This is expected from the Rabi chevron pattern for each qubit (Fig. 2a) because the separation between the set target frequency range (50 MHz) is larger than the width of each chevron pattern (~10 MHz). In contrast, simultaneous qubit operation generally reduces T_{Rabi} and oscillation visibility. The time required for the Bayesian calculation depends on the type of operation mode. It takes 10 μs for the single-qubit probe-feedback mode and two-qubit probe-only mode. However, it takes 50 μs for the two-qubit probe-feedback mode, leading to ~70 shots × 65 μs = 4.6 ms of latency per Hamiltonian estimation. This is because of the limited resources available on the FPGA setup for parallel computations. Thus, we ascribe the reduced T_{Rabi} to the increased latency for simultaneous Bayesian estimation and frequency feedback, during which the uncertainty of the estimation increases owing to the diffusion of ΔB_z. In addition, reduced oscillation visibility is induced by the finite readout crosstalk between two qubits (see Supplementary Note 3).

Furthermore, we performed a simultaneous Ramsey interference of two qubits by applying calibrated π/2 pulses separated by t_W and by varying δf, as shown in Fig. 2c. We then extract $T_2^* \approx 151(183)$ns for Q_L (Q_R) (inset of Fig. 3c), by fitting the Ramsey amplitude decay to a Gaussian function at each resonant frequency[20]. There is room for further improvements in T_2^* by increasing computational resources of the FPGA setup and removing the readout crosstalk, using newly developed machine learning techniques[35], for example. Nevertheless, we keep these tasks for future work.

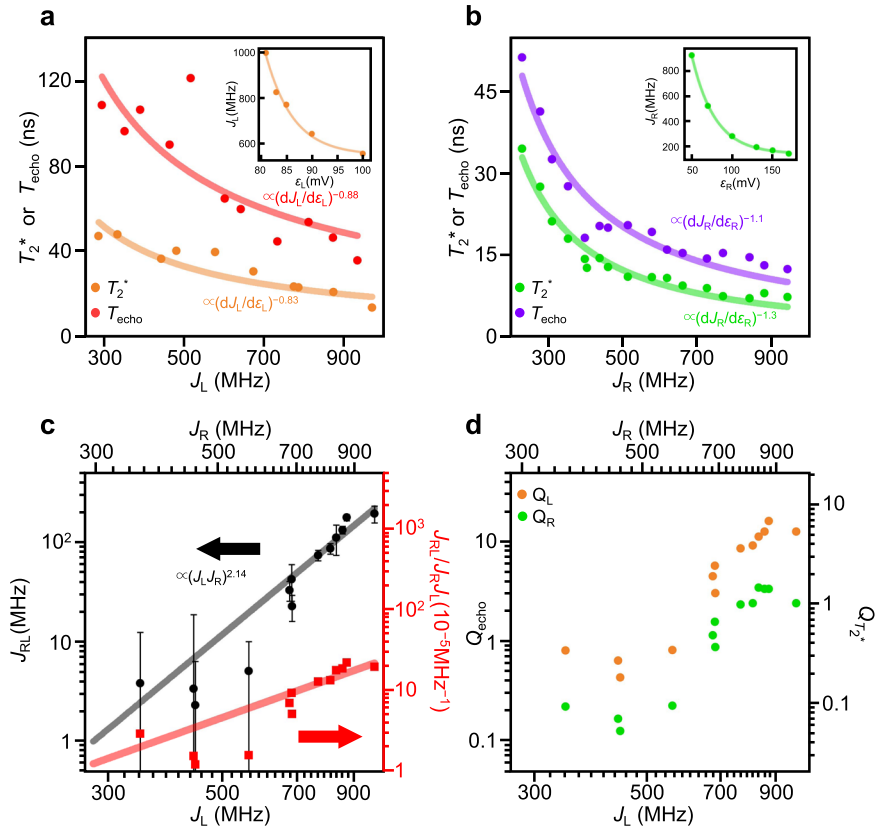

Fig. 4 Super-linearly increasing the inter-qubit coupling strength. a, **b** T_2* and T_{echo} of Q_L(Q_R). The solid curves are fit to the forms $(dJ/d\varepsilon)^{-b}$ with best fit parameter $b \approx 1.0$. Inset: the intra-qubit exchange energy of each qubit as a function of detuning amplitude ε. The solid line denotes an exponential fit of a form $J(\varepsilon) = J_0 + J_1 \exp((\varepsilon_0 - \varepsilon)/\alpha)$. **c** J_{RL} (black circle) and J_{RL}/J_LJ_R (red square) as a function of J_L and J_R. The black solid line is a fit to $J_{RL} = a(J_LJ_R)^{\alpha}$ with the best fit parameter $\alpha = 2.14$ indicating super-linear behavior. The error bars are estimated from the fitting uncertainty. **d** The conditional phase-flip quality factors $Q_{T_2^*}$ and Q_{echo} of Q_L (orange circle) and Q_R (green circle).

Capacitive coupling between two ST_0 qubits

We now discuss the two-qubit capacitive-coupling measurements using the dual Hamiltonian estimation circuit discussed in the previous section. Specifically, throughout the experiment, a resonant RF pulse is applied to the control qubit to observe the state-dependent frequency shift of the target qubit, whose frequency is estimated by the Hamiltonian estimator. In addition, using the simultaneous Hamiltonian estimation circuit, the control qubit is operated when the separation between the qubit frequency is larger than 50 MHz to prevent the unwanted flip of the target qubit by the RF crosstalk.

The capacitive coupling between singlet–triplet qubits originates from the different electric dipole moments of states $|S\rangle$ and $|T_0\rangle$ (ref. [36]). It has been considered to be a simple method to generate leakage-free two-qubit gates[22,26,27,37] unlike the inter-qubit exchange coupling-based method, in which the inter-qubit magnetic field difference should be sizable to prevent leakage of the qubits outside the computational space[22]. Nevertheless, the weak coupling dependent on the intra-qubit exchange energies constitutes the main disadvantage of the capacitive-coupling method. For example, the pioneering demonstration of entanglement in GaAs[26] used a coupling strength on the order of a few MHz, whereas individual exchange energies were approximately 300 MHz. Moreover, it has been assumed that capacitive coupling follows a bilinear form $J_{RL} \propto J_LJ_R$. In this bilinear form, the entanglement fidelity is expected to remain constant since the fidelity is limited by the dephasing of an individual qubit in $J_{RL} << J_{L(R)}$, giving a constant quality factor for $T^*_{2L(R)} \propto \left(J_{L(R)}\right)^{-1}$ (ref. [26]). This constant entanglement fidelity is experimentally confirmed in previous research, indicating that the bilinear form seems to hold, at least for the experiment in which the inter-qubit distance is larger than the distance between dots within a qubit[26,36].

The validity of the previously assumed scaling of J_{RL} was experimentally tested in a regularly and compactly spaced linear QD array. Motivated by theoretical works showing that J_{RL} can actually be a stronger function of J_L and J_R (ref. [37]), we measured J_{RL} by performing state-dependent exchange oscillation in combination with the dual Hamiltonian estimator. Figure 3a shows the pulse sequence for the target and control qubits. After the probe step, the control qubit is initialized to the x axis of a Bloch sphere, followed by an optional π pulse. J_{RL} is then adiabatically switched on by slowly adjusting the detuning of the control qubit while the target qubit is initialized to the x axis of a Bloch sphere. The exchange oscillation of the target qubit is then performed by diabatically changing the detuning of the target qubit for a time t_{exch} to induce exchange oscillations, whose frequency depends on the control qubit state as $f^T = \sqrt{(J^T - J_{RL}r_C)^2 + \Delta B_z^2}$ according to Eq. (1), where J^T is the intra-qubit exchange energy of the target qubit and $r_C = 0$ (1) when the state of the control qubit is $|S\rangle(|T_0\rangle)$.

Figure 3b (Fig. 3c) shows the resultant state-conditional frequency shift of Q_L (Q_R) as a function of t_{exch}, with $J_{R(L)}$ ~3.61 (4.13) GHz. The precession frequency of the qubit is lower when the control qubit is in the $|S\rangle$ state for both cases, which is consistent with the charge configuration of the QD array[38]. The observed frequency shifts of 34.9 (40.6) MHz for Q_L (Q_R) is a direct measure of J_{RL}, which is significantly larger than the value

reported in (ref. [38]). As predicted in recent theoretical works, we hypothesize that the different relative orientations and the shorter distance between the qubits are related to this enhancement[39]. In addition, we observe the beating of the target qubit oscillation when the control qubit is prepared as a superposition of $|S\rangle$ and $|T_0\rangle$ (see Supplementary Note 4).

We also measured T_2* and spin-echo coherence time, T_{echo}, for each qubit to quantify the quality factor of the conditional phase-flip operation. Figure 4a, b shows T_2* and T_{echo} for each qubit, where T_2* is extracted from the exponentially decaying exchange oscillation and T_{echo} is measured by fitting the data to the echo envelope using calibrated π/2 and π pulses. Along with the form $J \propto \exp(-\varepsilon)$ (inset of Fig. 4a, b), we observe charge noise-limited coherence time, where T_2* and T_{echo} are close to the form $(dJ/d\varepsilon)^{-1}$ (ref. [20]). This essentially explains why previously demonstrated entanglement quality showed no improvement when increasing J_L and J_R if $J_{RL} \propto J_L J_R$ (ref. [26]).

Next, we perform the experiment in Fig. 3 with varying J_L and J_R near $J_R = J_L$ to investigate the super-linearity of J_{RL} when both qubits show reasonable coherence. Figure 4c shows the nonlinear behavior of J_{RL} as J_L and J_R increase, manifesting the deviation from the bilinear proportionality[26,27] in our device. Here, the error bar of the estimated J_{RL} is determined by the fitting uncertainty limited by the sampling rate of the arbitrary waveform generator (see Supplementary Note 5). By fitting the measured J_{RL} to $(J_L J_R)^a$, the agreement with experimental data is found for $a = 2.14$, which is close to the theoretically expected form $J_{RL} \sim (J_L J_R)^2$ using the effective Hamiltonian obtained from a Hund–Mulliken model independent of the details of the confinement potential in the regime where intra-qubit tunnel coupling overwhelms the intra-qubit exchange energy[37] (see Supplementary Note 6). Moreover, we estimated the dipolar energy $D \approx 46$ GHz, the order of which is consistent with the recent experimental work using a similar interdot spacing[40]. With this super-linear proportionality, we observe $J_{RL} > 190$ MHz when J_L and $J_R \approx 900$ MHz, showing that more than 20% of the state-conditional qubit frequency shift can be obtained in a closely spaced QD array.

DISCUSSION

The nonlinear $J_{RL}(J_L, J_R)$ form implies that the two-qubit gate quality should increase at larger J_L and J_R. We calculated $Q_{T_2*(echo)} \equiv 2JT_2 * (T_{echo})$, which quantifies the number of conditional phase flips within T_2*(T_{echo}), as shown in Fig. 4d. We observed Q_{echo} as high as ~16 (~7) for Q_L (Q_R), predicting that the fidelity of a conditional phase-flip operation of Q_L (Q_R) with Q_R (Q_L) in the σ_z eigenstate reaches as high as $e^{-1/Q_{echo}} = 94.0(86.7)\%$ and also monotonically increases as a function of J_L and J_R. In addition, the simulation based on the measured values predicts that the maximum attainable Bell state fidelity F_{Bell} reaches ≈95% and increases at larger J_L and J_R, where the Bell state is prepared by the echo-like pulse implemented in ref. [26] in which F_{Bell} maximizes at ≈72% with $J_{RL} \approx 1$ MHz(see Supplementary Note 7).

Previously, a Bell state fidelity with a capacitive coupling has enhanced to ≈93% with simultaneous rotary echo and rapid dynamic nuclear polarization (DNP), which enabled an approximately tenfold increase of a coherence time with $\Delta B_z = 900$ MHz, but J_{RL} on the order of a few MHz was rather exploited[27]. Thus we expect that F_{Bell} could be enhanced more by applying simultaneous rotary echo to the closely spaced QD array at a large J_{RL}, although the application is not currently viable in our device due to the insufficient DNP rate. In addition, the minimum time step and pulse rise times are currently limited by the sample rate of the waveform generator (2.4 Gsa/s), which also prevents performing full two-qubit gate operations and entanglement demonstration. Therefore further optimization with a faster signal source is still required. Note also that the pulse sequence in Fig. 3a is proper only for a two-qubit interaction measurement since the control qubit is likely to decohere while adiabatically turning on the interaction. Thus, a different qubit driving strategy (for example, using a non-adiabatic pulse) should be devised for entanglement demonstration, which will be considered in future work. Nonetheless, as our Hamiltonian estimation technique and readout method are compatible with large ΔB_z, we anticipate that performing a full two-qubit experiment in a regularly and closely spaced linear QD array, with increased ΔB_z by micromagnets or dynamic nuclear polarization, may show an even higher two-qubit gate fidelity that is also fast, exploiting large J_{RL}.

In conclusion, we demonstrated the simultaneous Hamiltonian parameter estimation and active suppression of the quasi-static noise of two ST_0 qubits in a GaAs quadruple QD array. Using fast qubit calibration routines, we also showed that both the magnitude and scaling of the capacitive coupling in a closely spaced QD array can be stronger than the previously measured bilinear form, leading to a state-conditional frequency shift of over 20 % and a quality factor of conditional phase flip of over 16. Our measurement confirms recent theoretical calculations and supports the possibility of realizing a high-fidelity and fast entanglement of encoded spin qubits in both GaAs and Si using a simple capacitive interaction.

METHODS

Device fabrication

The quadruple QD device shown in Fig. 1a was fabricated on a GaAs/AlGaAs heterostructure where two-dimensional electronic gas (2DEG) is located 70 nm below the surface. Mesa was defined by a wet etching technique to eliminate 2DEG outside the region of interest to suppress unwanted leakage. Five ohmic contacts were formed by metal diffusion with thermal annealing. Nanogates were fabricated by e-beam lithography and metal evaporation.

Measurement

The device was placed on the 7 mK plate in a commercial dilution refrigerator (Oxford Instruments, Triton-500). The battery-operated voltage sources (Stanford Research Systems, SIM928) supplied by stable DC voltages rapid voltage pulses generated by the arbitrary waveform generator with the maximum sampling rate of 2.4 Gsa/s (Zurich Instruments, HDAWG) were applied to metallic gates through on-board bias-tees. A detailed description of the experimental setup and FPGA implementation can be found in Supplementary Note 2.

DATA AVAILABILITY

The data that support the findings of this study are available from the corresponding author upon request.

Received: 8 November 2022; Accepted: 10 March 2023;
Published online: 29 March 2023

REFERENCES

1. Loss, D. & DiVincenzo, D. P. Quantum computation with quantum dots. *Phys. Rev. A* **57**, 120 (1998).
2. Yoneda, J. et al. A quantum-dot spin qubit with coherence limited by charge noise and fidelity higher than 99.9%. *Nat. Nanotechnol.* **13**, 102–106 (2018).
3. Mills, A. R. et al. Two-qubit silicon quantum processor with operation fidelity exceeding 99%. *Sci. Adv.* **8**, eabn5130 (2022).
4. Shulman, M. D. et al. Suppressing qubit dephasing using real-time Hamiltonian estimation. *Nat. Commun.* **5**, 1–6 (2014).
5. Fedele, F. et al. Simultaneous operations in a two-dimensional array of singlet-triplet qubits. *PRX Quantum* **2**, 040306 (2021).

6. Hendrickx, N. W. et al. A four-qubit germanium quantum processor. *Nature* **591**, 580–585 (2021).
7. Takeda, K. et al. Quantum tomography of an entangled three-qubit state in silicon. *Nat. Nanotechnol.* **16**, 965–969 (2021).
8. Philips, S. G. et al. Universal control of a six-qubit quantum processor in silicon. *Nature* **609**, 919–924 (2022).
9. Petit, L. et al. Universal quantum logic in hot silicon qubits. *Nature* **580**, 355–359 (2020).
10. Yang, C. H. et al. Operation of a silicon quantum processor unit cell above one kelvin. *Nature* **580**, 350–354 (2020).
11. Camenzind, L. C. et al. A hole spin qubit in a fin field-effect transistor above 4 kelvin. *Nat. Electron.* **5**, 178–183 (2022).
12. Harvey-Collard, P. et al. Coherent spin-spin coupling mediated by virtual microwave photons. *Phys. Rev. X* **12**, 021026 (2022).
13. Mi, X. et al. A coherent spin–photon interface in silicon. *Nature* **555**, 599–603 (2018).
14. Taylor, J. M. et al. Relaxation, dephasing, and quantum control of electron spins in double quantum dots. *Phys. Rev. B* **76**, 035315 (2007).
15. Coish, W. A. & Loss, D. Singlet-triplet decoherence due to nuclear spins in a double quantum dot. *Phys. Rev. B* **72**, 125337 (2005).
16. Petta, J. R. et al. Coherent manipulation of coupled electron spins in semiconductor quantum dots. *Science* **309**, 2180–2184 (2005).
17. Malinowski, F. K. et al. Spectrum of the nuclear environment for GaAs spin qubits. *Phys. Rev. Lett.* **118**, 177702 (2017).
18. Kha, A., Joynt, R. & Culcer, D. Do micromagnets expose spin qubits to charge and Johnson noise? *Appl. Phys. Lett.* **107**, 172101 (2015).
19. Kawakami, E. et al. Gate fidelity and coherence of an electron spin in an Si/SiGe quantum dot with micromagnet. *Proc. Natl Acad. Sci. USA* **113**, 11738–11743 (2016).
20. Dial, O. E. et al. Charge noise spectroscopy using coherent exchange oscillations in a singlet-triplet qubit. *Phys. Rev. Lett.* **110**, 146804 (2013).
21. Meunier, T., Calado, V. E. & Vandersypen, L. M. K. Efficient controlled-phase gate for single-spin qubits in quantum dots. *Phys. Rev. B* **83**, 121403 (2011).
22. Srinivasa, V. & Taylor, J. M. Capacitively coupled singlet-triplet qubits in the double charge resonant regime. *Phys. Rev. B* **92**, 235301 (2015).
23. Nakajima, T. et al. Coherence of a driven electron spin qubit actively decoupled from quasistatic noise. *Phys. Rev. X* **10**, 011060 (2020).
24. Sergeevich, A., Chandran, A., Combes, J., Bartlett, S. D. & Wiseman, H. M. Characterization of a qubit Hamiltonian using adaptive measurements in a fixed basis. *Phys. Rev. A* **84**, 052315 (2011).
25. Hirose, M. & Cappellaro, P. Coherent feedback control of a single qubit in diamond. *Nature* **532**, 77–80 (2016).
26. Shulman, M. D. et al. Demonstration of entanglement of electrostatically coupled singlet-triplet qubits. *Science* **336**, 202–205 (2012).
27. Nichol, J. M. et al. High-fidelity entangling gate for double-quantum-dot spin qubits. *NPJ Quantum Inf.* **3**, 1–5 (2017).
28. Kim, J. et al. Approaching ideal visibility in singlet-triplet qubit operations using energy-selective tunneling-based Hamiltonian estimation. *Phys. Rev. Lett.* **129**, 040501 (2022).
29. Jang, W. et al. Robust energy-selective tunneling readout of singlet-triplet qubits under large magnetic field gradient. *NPJ Quantum Inf.* **6**, 1–7 (2020).
30. Elzerman, J. M. et al. Single-shot read-out of an individual electron spin in a quantum dot. *Nature* **430**, 431–435 (2004).
31. Dehollain, J. P. et al. Bell's inequality violation with spins in silicon. *Nat. Nanotechnol.* **11**, 242–246 (2016).
32. Kandel, Y. P. et al. Coherent spin-state transfer via Heisenberg exchange. *Nature* **573**, 553–557 (2019).
33. Qiao, H. et al. Coherent multispin exchange coupling in a quantum-dot spin chain. *Phys. Rev. X* **10**, 031006 (2020).
34. Takeda, K. et al. Optimized electrical control of a Si/SiGe spin qubit in the presence of an induced frequency shift. *NPJ Quantum Inf.* **4**, 1–6 (2018).
35. Duan, P. et al. Mitigating crosstalk-induced qubit readout error with shallow-neural-network discrimination. *Phys. Rev. Appl.* **16**, 024063 (2021).
36. Taylor, J. M. et al. Fault-tolerant architecture for quantum computation using electrically controlled semiconductor spins. *Nat. Phys.* **1**, 177–183 (2005).
37. Buterakos, D., Throckmorton, R. E. & Sarma, S. D. Simulation of the coupling strength of capacitively coupled singlet-triplet qubits. *Phys. Rev. B* **100**, 075411 (2019).
38. Van Weperen, I. et al. Charge-state conditional operation of a spin qubit. *Phys. Rev. Lett.* **107**, 030506 (2011).
39. Hiltunen, T. & Harju, A. Capacitative coupling of singlet-triplet qubits in different interqubit geometries. *Phys. Rev. B* **90**, 125303 (2014).
40. Neyens, S. F. et al. Measurements of capacitive coupling within a quadruple-quantum-dot array. *Phys. Rev. Appl.* **12**, 064049 (2019).

ACKNOWLEDGEMENTS

This work was supported by the National Research Foundation of Korea (NRF) grant funded by the Korean Government (MSIT) (No. 2018R1A2A3075438, No. 2019M3E4A1080144, No. 2019M3E4A1080145, and No. 2019R1A5A1027055), Korea Basic Science Institute (National Research Facilities and Equipment Center) grant funded by the Ministry of Education (No. 2021R1A6C101B418), and Creative-Pioneering Researchers Program through Seoul National University (SNU). The cryogenic measurement used equipment supported by the Samsung Science and Technology Foundation under Project Number SSTF-BA1502–03.

AUTHOR CONTRIBUTIONS

D.K. and J.Y. conceived the project. J.Y. performed the measurements and analyzed the data. J.K. and H.J. fabricated the device. J.P., H.J., W.J., Y.S., M.C., and H.S. built the experimental setup and configured the measurement software. V.U. synthesized and provided the GaAs heterostructure. All the authors contributed to the preparation of the manuscript.

COMPETING INTERESTS

The authors declare no competing interests.

ADDITIONAL INFORMATION

Supplementary information The online version contains supplementary material available at https://doi.org/10.1038/s41534-023-00699-4.

Correspondence and requests for materials should be addressed to Dohun Kim.

Reprints and permission information is available at http://www.nature.com/reprints

Publisher's note Springer Nature remains neutral with regard to jurisdictional claims in published maps and institutional affiliations.